JOURNAL OF CATALYSIS **169,** 516–526 (1997)
ARTICLE NO. CA971706

Structure and Properties of Tungstates Formed in W–Mg–O Systems

C. Martín,*,[1] P. Malet,† V. Rives,*,[1] and G. Solana*,[2]

*Departamento de Química Inorgánica, Universidad de Salamanca, Salamanca, Spain; and †Departamento de Química Inorgánica, Instituto de Ciencia de Materiales, Centro Mixto CSIC-Universidad de Sevilla, Sevilla, Spain

Received January 23, 1997; revised March 17, 1997; accepted March 17, 1997

New W–Mg–O systems have been obtained by impregnation of MgO with aqueous ammonium paratungstate solutions. The systems have been characterized by X-ray diffraction, Raman and W L_3 X-ray absorption (XAS) spectroscopies, FT-IR monitoring of pyridine adsorption for surface acidity, nitrogen adsorption at 77 K, and electron microscopy. Results obtained indicate that amorphous Mg tungstates are formed for low (723 K) calcination temperatures, but crystalline compounds are formed after calcination above 973 K. W^{6+} coordination in these solids depends on W content and calcination temperature. So, tetrahedral [WO_4] species exist in amorphous species with low W content, and the crystalline ones obtained after calcination at 973 or 1073 K, while octahedral [WO_6] species are present in amorphous solids with large (24 wt%) W content and in the crystalline phases formed after calcination at 1273 K. Formation of tungstates at rather low calcination temperature arises from the strong acid/base interaction between both reactants. Incorporation of tungsten leads to development of surface Lewis acid sites. The tungsten-containing species are less reducible in all cases than bulk WO_3.

1. INTRODUCTION

It is well established that when oxides are supported on other oxides, the reactivity properties are highly dependent on the preparation method, calcination process, the presence of doping agents, type of support, etc. (1, 2). Tungsten oxide-containing catalysts are widely used in several industrial catalytic reactions, such as isomerization, and metathesis of alkenes, alcohol dehydrogenation, hydrodesulfurization, and hydrocracking of oil heavy fractions, etc. (3–7). Magnesium oxide, pure or mixed with other oxides, is used in hydrocarbon dehydrogenation (8, 9), although, because of its rather low specific surface area it had been scarcely used as a catalyst support, the fact that this specific surface area can be increased through reaction with water and further dehydration, has made it very attractive as a catalyst support in recent years.

Despite the huge literature regarding tungsten-containing catalysts, the WO_3–MgO system has not deserved much attention, although the high basicity of the support makes this system potentially different from the most commonly studied systems, i.e., tungsta supported on silica, titania, or alumina (1–5, 10–14).

In this paper we report on the preparation and properties of WO_3–MgO systems possessing different tungsten loadings and calcined at several temperatures. They have been characterized using a large selection of physicochemical techniques, in order to attain a complete description of these systems.

2. EXPERIMENTAL

2.1. Samples Preparation

Two series of W–Mg–O samples have been prepared, using two types of magnesia supports: commercial MgO (periclase, from Panreac, Spain, with a specific surface area of 63 $m^2\ g^{-1}$) and $Mg(OH)_2$ (brucite), obtained from MgO by impregnation in water and calcination at 723 K in air for 3 h (support MgOT, with a specific surface area of 218 $m^2\ g^{-1}$). Tungsten was incorporated by impregnation of the respective support with aqueous solutions of ammonium paratungstate (Fluka, Germany). After drying at 373 K for 10 h in air, the samples were calcined in air at temperatures ranging from 723 to 1273 K for 3 h. The tungsten content ranges from 5 to 24 wt%. Some samples were prepared containing up to 60 or even 80 wt%, although these samples were analyzed only by X-ray diffraction. The general properties of the samples studied are summarized in Table 1. They are named WMA or WMTA (A standing for W weight percentage), when prepared on supports MgO or MgOT, respectively. When the calcination temperature was different from 723 K, it is also given (i.e., WM9/1173 stands for a sample containing 9% W, prepared on support MgO and calcined at 1173 K).

2.2. Experimental Techniques

X-ray diffraction (XRD) profiles were recorded in a Siemens D-500 instrument, using Ni-filtered Cu$K\alpha$1

[1] To whom correspondence should be addressed.
[2] On leave from Universidad de Guanajuato, Guanajuato, México.

0021-9517/97 $25.00

TABLE 1

Tungsten Content, Calcination Temperature, Specific Surface Area, and Crystalline Phases in the Supports and the Catalysts Studied

Sample	wt% W	Calcination temperature (K)	S_{BET} ($m^2\ g^{-1}$)	Crystalline phases[a]
MgO	—	723	63	P
MgOT	—	723	218	B
WM5	5	723	250	P
WM9	9	723	245	P
WM18	18	723	153	P
WM24	24	723	150	P
WMT24	24	723	191	P
WM9/1173	9	1173	30	P + MWx
WM24/1073	24	1073	75	P + MW(I)
WM24/1273	24	1273	18	P + MW(II)
WMT24/1073	24	1073	85	P + MW(I)
WMT24/1273	24	1273	24	P + MW(II)

[a] As determined by X-ray diffraction: P, periclase; B, brucite; MWx, nonstoichiometric magnesium tungstate; MW(I), $MgWO_4$(I), corresponding to JCPDS file 19-776; MW(II), $MgWO_4$(II), corresponding to wolframite, JCPDS file 27-789.

radiation ($\lambda = 154.05$ pm) interfaced to a DACO-MP data acquisition microprocessor equipped with Diffract/AT software.

Nitrogen adsorption isotherms at 77 K for surface area and porosity determination were measured in a conventional high vacuum pyrex system (residual pressure 10^{-4} N m^{-2}), pressure changes being monitored with a MKS pressure transducer.

The Raman spectra in the 200–1200 cm^{-1} range were recorded on a computer-controlled Jobin Ybon spectrometer, Model U-1000, using the 514.5-nm line from a Spectra Physics Model 165 Ar^+ laser as the exciting source; the spectra shift-width was typically of 5 cm^{-1}, and laser source powers of ca. 400 mW, measured at the sample, were used.

Scanning electron microscopy (SEM) images of the samples were obtained with a Zeiss DSM940 digital scanning microscope between 20 and 30 kV with magnifications between 1000 and 10,000. The maximum resolution was 5 nm at 30 kV. Samples were sputtered with gold for 150 s using a Bio-Rad SEM loading instrument, working a 1.6 kV and 25 mA.

X-ray absorption (XAS) data at the W L_3 edge were collected at 77 K on wiggler station 9.2 at the Daresbury Synchrotron Radiation Source (UK) with an electron ring running at 2 GeV and 210–230 mA. Monochromatization was obtained with a double silicon crystal monochromator working at the (220) reflection, which was detunned 50% to minimize higher harmonics. The measurements were carried out in the transmission mode using optimized ion chambers as detectors. Sample powders, diluted with boron nitride when necessary, were ground, homogeneized, and pressed into self-supporting wafers, with a total absorbance ca. 2.5 above the W L_3 edge (10202 eV) and edge jumps just below 1.0. At least three scans were recorded and averaged in order to obtain experimental spectra. The EXAFS function $\chi(k)$ was obtained from the experimental X-ray absorption spectrum by conventional procedures (15). Theoretical backscattering amplitude and phase shift functions for W–W and W–Mg absorber-backscatterer pairs were calculated by using the program FEFF (16), while experimental functions for W–O absorber-backscatterer pairs were extracted from the spectrum of $Al_2(WO_4)_3$, a compound where W^{6+} cations are surrounded (17) by four oxygen atoms at 1.78 ± 0.03 Å (forward Fourier transform, k^3-weighted, $\Delta k = 2.4$–15.5 $Å^{-1}$; inverse Fourier transform, $\Delta R = 0.6$–2.2 Å). EXAFS data analyses were performed by using the programme package NEWEXAFS (University of Eindhoven, The Netherlands).

Temperature-programmed reduction (TPR) analysis was carried out in a Micromeritics TPR/TPD 2900 instrument, at a heating rate of 10 K/min and using ca. 15 mg of sample and a H_2/Ar (5% vol) mixture (from Sociedad Española del Oxígeno, Spain) as reducing agent (60 ml min^{-1}); experimental conditions for TPR runs were chosen according to data reported elsewhere (18) in order to reach good resolution of the component peaks.

Adsorption of pyridine (for surface acidity measurements) was monitored by FT-IR spectroscopy, using a Perkin–Elmer 16PC spectrometer, connected to an Ataio 386-SX computer, using special cells with CaF_2 windows. Samples were submitted to a conditioning treatment *in situ*, consisting of outgassing at 673 K for 2 h (residual pressure 10^{-3} N m^{-2}) before the adsorption studies were performed.

3. RESULTS AND DISCUSSION

3.1. Surface Texture

Nitrogen adsorption–desorption isotherms on the supports and the samples studied are very similar. Some representative curves have been plotted in Fig. 1. They correspond to type II in the IUPAC classification, with an hysteresis loop in the 0.5–0.9 relative pressure (P/P_0) range, the loop corresponding to type H3 of this same classification (19), due to adsorption on mainly mesoporous samples.

The specific surface area values, as determined following the BET method, are given in Table 1. The sharp increase in the specific surface area when passing from the original support MgO (63 $m^2\ g^{-1}$) to tungsten-loaded samples (WM5, WM9, WM18, and WM24) is due to the presence of water during preparation of the samples. MgO easily reacts with water thorough the reversible reaction

$$\text{MgO (periclase)} \leftrightarrow \text{Mg(OH)}_2\text{ (brucite)}$$

leading to large specific surface area materials (20). For comparison, as mentioned above, another support (MgOT)

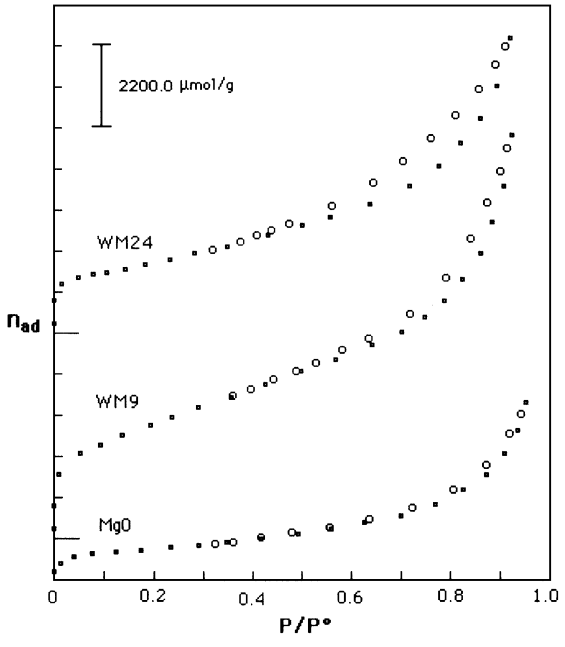

FIG. 1. Nitrogen adsorption–desorption isotherms (77 K) for support MgO and for samples WM9 and WM24. Filled points, adsorption data; empty points, desorption data.

has also been used, prepared by impregnation of commercial MgO in water and calcination at 723 K in air; in this case, the structure of the support, prior to tungsten incorporation, is that of brucite, $Mg(OH)_2$; the specific surface area of this support (Table 1) is of the same order as that shown by the tungsten-containing samples prepared by impregnation. When this large specific surface area support is impregnated with the aqueous tungstate solution and calcined, the specific surface area does not increase as for the original, commercial MgO support, but a slight decrease is observed (e.g., sample WMT24), in a similar way as that observed for other supports, such as silica, alumina, or titania, after supporting another oxide. For samples with the same W loading and the same calcination temperature, the specific surface area is always larger when prepared on support MgOT than that on support MgO.

Pore size distribution curves (Fig. 2) show the major presence of pores with diameter between 2 and 6 nm for original MgO. For low W loadings (sample WM9) the contribution to the surface area by large pores decreases, but when the W loading is increased, the contribution of these pores to the surface area increases as well.

3.2. X-Ray Diffraction

The crystalline phases identified in the different samples by X-ray diffraction are given in Table 1. No difference was found between the XRD diagrams of samples prepared on supports MgO and MgOT; so, the discussion and plots following mostly refer to samples prepared on MgO.

All X-ray diffraction diagrams for samples containing less than 60 wt% W, calcined at 723 K, show (Fig. 3) intense diffraction peaks due to MgO, periclase, at 243.1 pm, planes (111), 210.6 pm (200), and 149.1 pm, planes (220). The only difference from the diagram for the original support is an increase in the width of the signals, indicating a decrease in crystallinity after incorporation of W. Actually, a straightforward relationship between the crystallinity of the solid before and after W incorporation cannot be established, as the impregnation step gives rise also to a change from periclase to brucite, while calcination leads to a further recovery of the periclase structure. The lack of diffraction peaks due to tungsten-containing species, even for rather high W loadings, indicates that these species are amorphous or as very small crystallites with $d < 4$ nm. For those samples prepared from support MgOT, no diffraction peak due to brucite was detected after calcination at 723 K, indicating that tungsten somewhat favors its change to periclase, a phase change observed, for pure brucite, at 773 K (21).

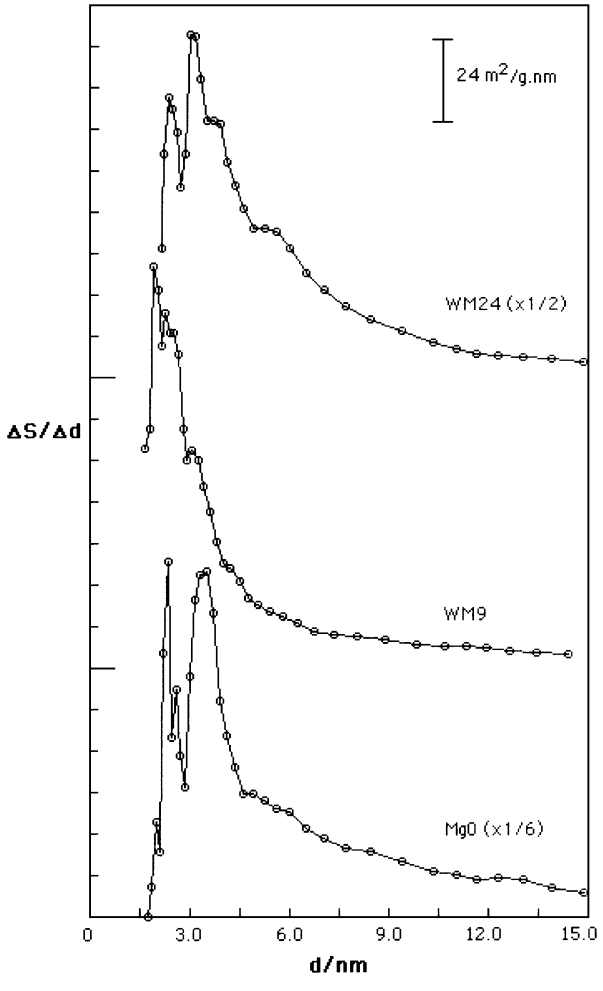

FIG. 2. Pore size distribution curves for support MgO and for samples WM9 and WM24.

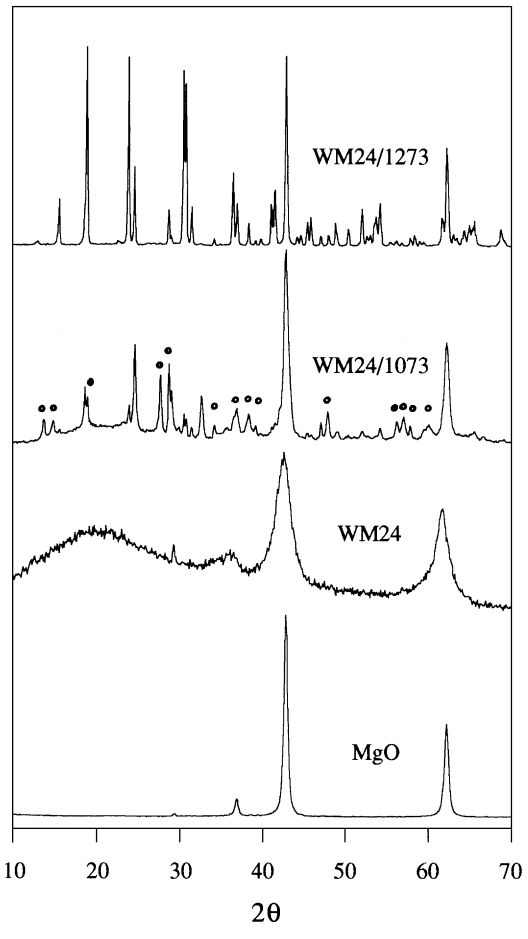

FIG. 3. X-ray diffraction patterns for support MgO and for samples WM24, WM24/1073, and WM24/1273. Circles, $MgOWO_4$(I), JCPDS file 19-776; unmarked peaks in the profile of sample WM24/1073 correspond to nonstoichiometric W–Mg–O compounds.

The X-ray diffraction diagram recorded for samples containing 24% W calcined at 1073 K (samples WM24/1073 and WMT24/1073) are rather complex, most of the diffraction lines coinciding with those of a high temperature (1438 K) stable magnesium tungstate, $MgWO_4$ (22), hereafter named $MgWO_4$(I). Similar diffraction diagrams have been reported upon dehydration of $MgWO_4 \cdot xH_2O$ at 423–923 K (23). However, both the structure of this low temperature dehydrated form and the high-temperature stable form are unknown, although the dehydration process is described as a topotactic one, tungsten being tetrahedrally coordinated and magnesium octahedrally coordinated in the hydrated form.

When the calcination temperature is increased (samples WM24/1173 and WMT/1173), new diffraction lines develop in the diagram, which coincide with those of crystalline $MgWO_4$ wolframite (file 27-789 of JCPDS), hereafter named $MgWO_4$(II), where both W and Mg are octahedrally coordinated. Some other weak peaks are also detected, specially for samples containing between 5–18% W (sample WM9/1173), not coinciding with any magnesium tungstate previously described in the literature; these peaks (4.763, 3.602, 3.103, 2.913, 2.735, and 1.925 Å) can be tentatively ascribed to nonstoichiometric magnesium tungstate Mg_xWO_4. For samples with high W content calcined at 1273 K (WM24/1273 and WMT24/1273), the major phase, as detected by XRD (Fig. 3) is $MgWO_4$(II). For lower W contents (5–18%) the crystalline W–Mg–O phases are detected only after calcination at high temperatures (at or above 1173 K). On the contrary, very high loaded samples (higher than 60% W) show XRD diagrams (Fig. 4) with diffraction lines due mainly to nonstoichiometric tungstates even after calcination at 373 K; as the calcination temperature of this is increased, lines due to $MgWO_4$(I) and $MgWO_4$(II), wolframite, develop, wolframite being the major component after calcination at 1173 K. It should be noted that no diffraction peak due to MgO was detected in these samples.

3.3. Laser Raman Spectroscopy

The Raman spectra of metal oxides provide a detailed information about their structure, as the Raman vibrational modes are determined by the type of symmetry and the structure of these compounds. The position of the fundamental band recorded at the highest wavenumbers position usually provides information about the M–O bond order.

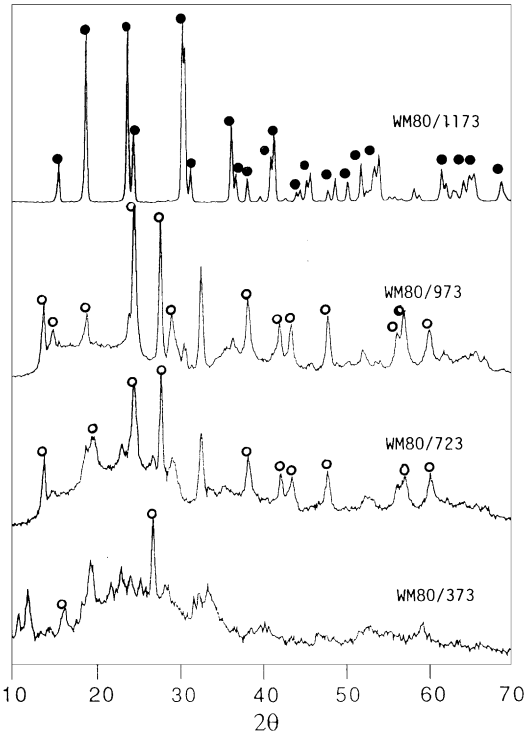

FIG. 4. X-ray diffraction profiles of high W-containing samples. Solid circles, $MgWO_4$(II), JCPDS profile 27-789; empty circles, $MgWO_4$(I), JCPDS 19-776.

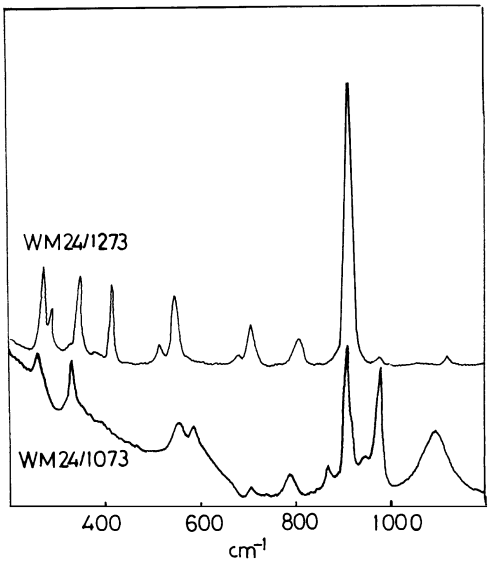

FIG. 5. Laser Raman spectra of samples WM24/1073 and WM24/1273.

From data in the literature for different tungstates with octahedral [WO_6] units ($FeWO_4$, $CoWO_4$, H_2WO_4, etc.) or tetrahedral [WO_4] units (Cs_2WO_4, $Fe_2(WO_4)_3$, etc.), it can be tentatively concluded that this band is recorded in the 910–1060 cm^{-1} range for tungstates containing [WO_4] units, while for those containing octahedral units the band is recorded below 980 cm^{-1}. However, distortions in [WO_4] or [WO_6] units modify the order bond, thus shifting the position of the band. Data in the literature generally assume (24) that only tetrahedral species give rise to the band above 980 cm^{-1}, while only octahedral units are responsible for the band below 910 cm^{-1}.

The Raman spectra of the low tungsten (less than 60 wt%) containing samples, calcined below 1073 K, show poorly defined bands, due to the presence of highly dispersed amorphous phases, their ascription to precise tungsten-containing moieties being rather unreliable.

On the contrary, samples with W contents larger than 18% calcined at 1073 K (samples WM24/1073 and WMT24/1073), show Raman spectra (Fig. 5) with bands at 793, 909, 980, and 1050 cm^{-1}. The positions of the first two bands coincide with those reported in the literature for crystalline wolframite, $MgWO_4$(II), which Raman spectrum shows intense bands at 800 and 911 cm^{-1}, and weak bands at 705, 546, 413, 234, and 271 cm^{-1} (25). However, in our case bands recorded at 980 and 1050 cm^{-1} suggest the simultaneous presence of tetrahedral [WO_4] units. Bands at 980 and 1050 cm^{-1} almost vanish in the spectrum of the sample calcined at 1273 K (sample WM24/1273), now showing bands at 914 (very strong), 810, 709, 550, 516, 418, 292, 275, and 251 cm^{-1}, almost coinciding with those reported in the literature for crystalline $MgWO_4$ (wolframite), the major species detected by XRD for this sample.

3.4. X-Ray Absorption Spectroscopy

The EXAFS spectra in the W L_3 absorption edge provide information regarding the local environment of tungsten in the amorphous compounds (undetected by X-ray diffraction) and in the $MgWO_4$(I) phase detected by XRD, similar to the reported phase stable at high temperature (1438 K); it should be noticed that despite the XRD diagram for this compound has been reported (23), the actual structure is unknown. For comparison purposes, the EXAFS spectrum in the W L_3 absorption edge has been also measured for the sample containing 24% W calcined at 1273 K, where the major crystalline component (as detected by XRD) is $MgWO_4$(II), with the wolframite structure.

3.4.1. Crystalline compounds (samples WM calcined at high temperatures). EXAFS oscillations at the W L_3 absorption edge for samples containing 24% W calcined at 1073 and 1273 K are shown in Fig. 6. It should be remembered that XRD analysis showed the presence of $MgWO_4$(I) and $MgWO_4$(II), wolframite, as the major components in these two samples, respectively.

The crystalline structure of wolframite $MgWO_4$ has been sketched in Fig. 7, according to literature crystallographic data for this compound (26). Tungsten ions form distorted octahedra [WO_6] (two oxide ions as 1.795 Å, two at 1.894 Å, and two at 2.140 Å), sharing edges to form chains. In its second coordinating sphere, each tungsten cation is surrounded by other two tungsten ions at 3.216 Å and eight

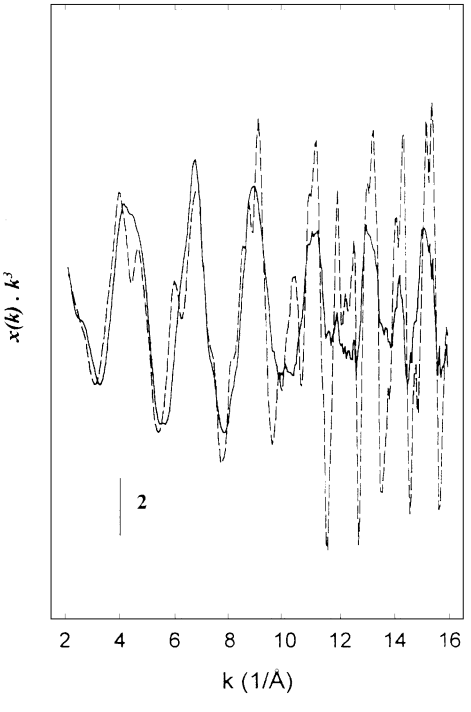

FIG. 6. EXAFS oscillations at the W L_3 edge for sample WM24 calcined at 1073 K (solid line) and 1273 K (dashed line).

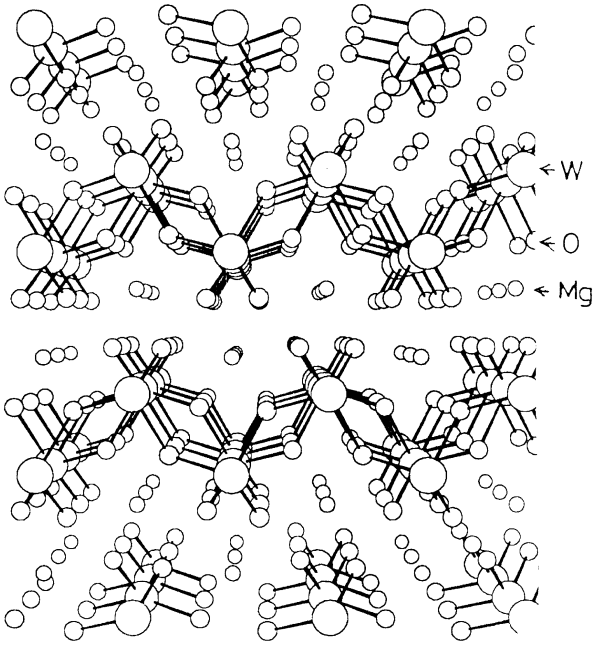

FIG. 7. Structure of $MgWO_4$ (wolframite).

TABLE 2

Best Fit Parameters for the EXAFS Spectrum of Sample WM24 Calcined at 1073 K [$MgWO_4$(I)] and 1273 K [$MgWO_4$(II)] and Samples WM9 and WM24 Calcined at 723 K

Sample	Atom	N	$\Delta\sigma^2$ (Å^2)	R (Å)	ΔE^0 (eV)
WM24/1073	O	4.4	0.0019	1.79	2.4
	W	0.5	0.0020	3.22	−9.9
	Mg	1.7	0.0025	3.48	−2.7
WM24/1273	O	4.4	0.0019	1.81	2.4
	O	1.7	0.0014	2.16	−5.2
	W	2.2	0.0016	3.22	−5.9
	Mg	3.4	0.0051	3.55	−8.2
WM9	O	4.1	0.0019	1.80	2.4
	Mg	1.9	0.0026	3.07	0.2
WM24	O	4.4	0.0019	1.81	2.4
	O	1.7	0.0014	2.18	−5.2
	W	1.7	0.0016	3.22	−5.9
	Mg	3.0	0.0051	3.53	−5.9

Note. Estimated errors for coordination numbers (N) and shell distances (R) are ±15% and ±0.02 Å, respectively.

Mg cations at 3.486–3.742 Å. EXAFS data for the sample with 24% W calcined at 1273 K can be fitted (Fig. 8A) with the structural parameters summarized in Table 2. In good agreement with the crystallographic data for wolframite, 6.1 ± 0.8 oxide ions are detected in two sublayers at 1.81 ± 0.02 and 2.16 ± 0.02 Å, while the second coordination sphere contains 2.2 ± 0.3 tungsten cations at 3.22 ± 0.02 Å, also in good agreement with data reported for wolframite. The larger misfit between the calculated and the reported coordination numbers and bond lengths arises from the coordination sphere containing Mg cations, probably due to the larger dispersion of distances in this coordination sphere.

This fit allows to ascribe the first two maxima in the uncorrected Fourier transform plot (Fig. 8A, maxima at ca.

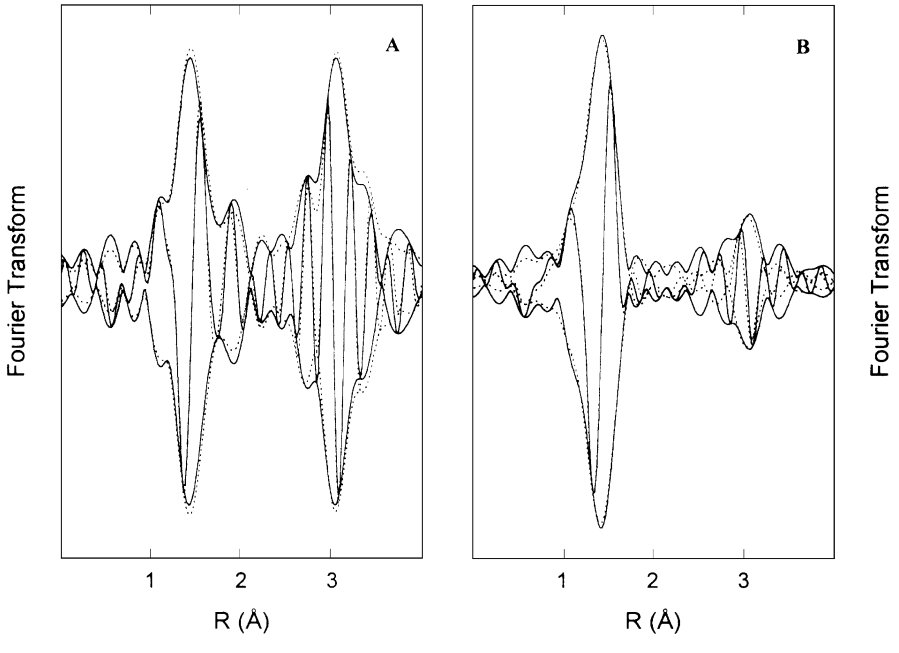

FIG. 8. Modulus and imaginary part of the k^3-weighted Fourier transform of the W L_3 EXAFS oscillations for samples WM24/1273 (A) and WM24/1073 (B). Solid lines, experimental data. Dashed lines, best fit functions ($\Delta k = 3$–15 Å^{-1} in all the Fourier transforms).

1.4 and 2 Å) to four short W–O bonds and two larger W–O bonds in the distorted [WO_6] octahedra; W–W bonds are the most important contribution to the maximum at 3 Å (uncorrected). The lower backscattering amplitude of Mg neighbors makes their contribution to the k^3-weighted Fourier transform markedly lower than the contribution due to the heavier W neighbors.

This ascription allows a qualitative interpretation of EXAFS data for $MgWO_4$(I), the major phase detected by XRD in samples containing 24% W and calcined at 1073 K (samples WM24/1073 and WMT24/1073) and which structure has not been determined from X-ray diffraction data. Thus, comparison of the k^3-weighted Fourier transforms for $MgWO_4$(I) and $MgWO_4$(II) (Fig. 8) shows that short W–O distances existing in wolframite persist in $MgWO_4$(I), while longer W–O distances have vanished. Simultaneously, the intensity of the maximum at 3 Å (without phase correction) has markedly decreased, indicating a much lower number of W neighbors at 3.22 Å.

Best fit parameters (Table 2, Fig. 8B) of EXAFS data for sample $MgWO_4$(I) confirm the conclusions reached above from a qualitative point of view. In this sample, W cations are coordinated by ca. 4 oxygen atoms and W–W distances at 3.22 Å have almost vanished. The presence of a weak contribution of neighbors W at 3.22 Å indicates that the phase obtained is not completely pure, but is mixed with small amounts of a phase closer to wolframite, $MgWO_4$(II). The shortest W–O bond distance, 1.79 ± 0.02 Å, coincides with that calculated in compounds where crystallographic data show the presence of tetrahedral units, such as $MgWO_4 \cdot 2H_2O$ (W–O distances 1.76–183 Å) (23). It should be stressed that this hydrated form leads, upon topotactic dehydration, to a material with an X-ray diffraction diagram very similar to that of $MgWO_4$(I), without W–W distances shorter than 4 Å, due to the lack of W–O–W bridges.

3.4.2. Amorphous phases (samples WM calcined at medium temperatures). No information could be concluded by X-ray diffraction nor Raman spectroscopy about the structures of the different amorphous phases existing in these samples. However, EXAFS spectra at the W L_3 edge provide information regarding the immediate W environment. Although spectra for different samples have been recorded, only those corresponding to samples WM9 and WM24 calcined at 723 K will be discussed.

Figure 9 shows EXAFS oscillations and their k^3-weighted Fourier transforms for sample WM9. Data for sample WM24/1073, where $MgWO_4$(I) had been detected by X-ray diffraction, have been included for comparison, showing that the local order around W cations in both samples is almost identical. So, we should conclude that sample WM9 contains mostly tetrahedral [WO_4] units. EXAFS data for sample WM24 are shown in Fig. 10, together with data corresponding to sample WM24/1273, where $MgWO_4$(II) had been detected by X-ray diffraction. Again, the local environment of W cations in both samples is very similar, and we should conclude that sample WM24 contains octahedral [WO_6] units, with a structure very similar to that of $MgWO_4$(II), in the first and higher coordination spheres.

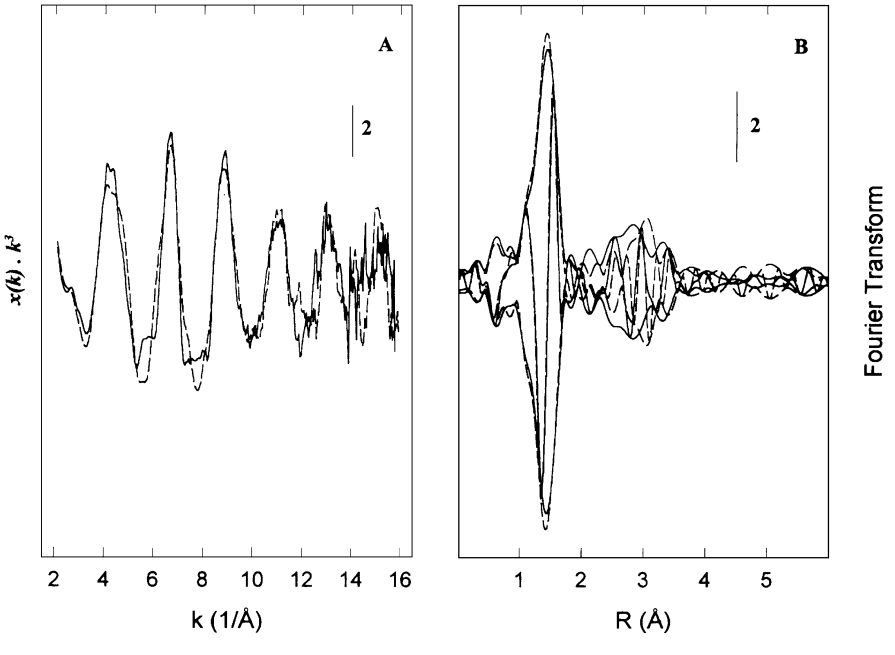

FIG. 9. W L_3 EXAFS oscillations (A) and associated k^3-weighted Fourier transform (B) for sample WM9 (solid lines). EXAFS data for sample WM24/1073 (dashed lines) have been included for comparison ($\Delta k = 2.4$–15.5 Å^{-1} in all the Fourier transforms).

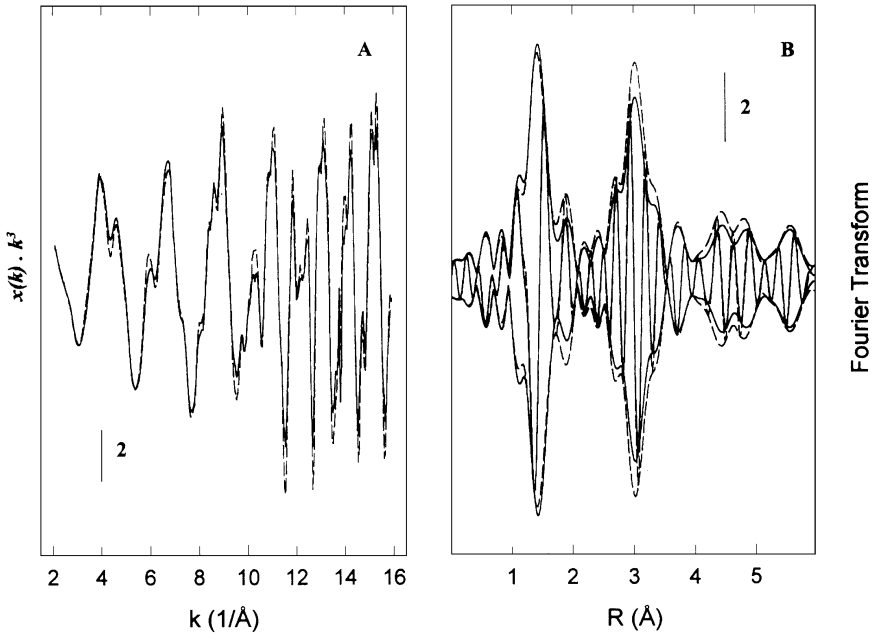

FIG. 10. W L_3 EXAFS oscillations (A) and associated k^3-weighted Fourier transform (B) for sample WM24 (solid lines). EXAFS data for sample WM24/1273 (dashed lines) have been included for comparison ($\Delta k = 2.4$–15.5 Å^{-1} in all the Fourier transforms).

The lack of diffraction lines corresponding to this compound in the profile of sample WM24 calcined at 723 K indicates that the particles are extremely small. Best fit parameters extracted from the EXAFS spectra of samples WM9 and WM24 are summarized in Table 2 and confirm the above qualitative conclusions. We should first notice that the local environment in the first coordination sphere of the W cations depends on the W loading. So, the coordination number is close to 4 for sample WM9, indicating a tetrahedral coordination, while an increase in the W content for sample WM24 leads to a sharp change in the first coordination sphere, leading to a coordination number close to 6, indicating the formation of distorted octahedral [WO_6] units, and to the raise of W–W distances characteristic of W–O–W bridges, also close to that existing in wolframite.

3.5. Temperature-Programmed Reduction

Temperature-programmed reduction profiles for selected samples are shown in Fig. 11. A decrease in reducibility (i.e., and increase in the threshold reduction temperature) is observed as the W content or the calcination temperature are increased; as mentioned above, both changes increase the crystallinity of the W-containing phases existing in the samples. A weak reduction process is observed below 1000 K that shifts toward higher temperatures as the precalcination temperature is increased, finally vanishing inside the band due to the main reduction process for sample calcined at 1073 K. This low-temperature band should be due to reduction of dispersed tungstates existing in the medium-temperature calcined samples, more easily reduced than the crystalline phases.

The reduction curves do not recover the base line in any case, even at the maximum temperature reachable by the apparatus, and so no precise quantitative analysis of the reduction process could be carried out. Even so, from the W content in the samples and the amount of hydrogen consumed in the temperature range 750–1100 K, the reduction

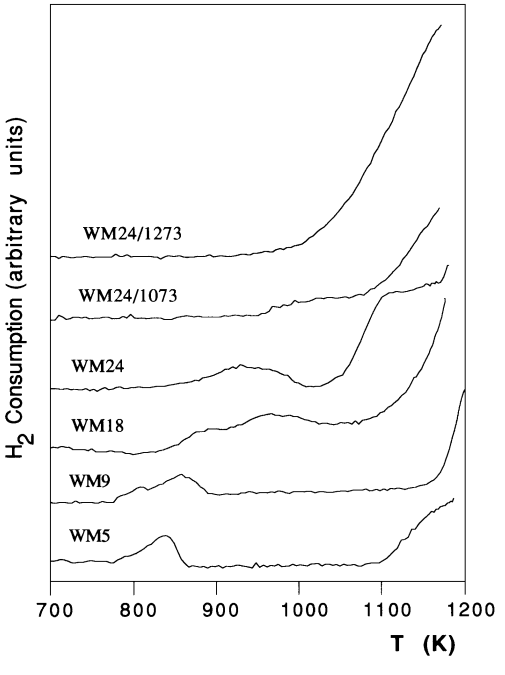

FIG. 11. Temperature-programmed reduction profiles for selected W–Mg–O samples.

percentage (assuming $W^{6+} \rightarrow W^0$) is always lower than 10%. This reducibility of the W–Mg–O samples is rather lower than that observed for bulk, crystalline WO_3 (27), and for tungsta supported on other metal oxides, such as silica, alumina or titania (7, 28), and should be attributed to the formation of W–Mg–O species that stabilize oxidation state +6 for tungsten.

3.6. Surface Acidity: Pyridine Adsorption

The FT-IR spectrum recorded after adsorption of pyridine (py) at room temperature on bare MgO shows intense absorption bands at 1442 and 1598 cm^{-1}, completely removed after outgassing at 373 K, suggesting that they correspond to physisorbed or weakly bonded py, probably through hydrogen bonding (29). However, the spectrum changes when the adsorption is carried out on the tungsten-containing samples (Fig. 12). The bands recorded become stronger and shift toward higher wavenumbers, as the W content is increased: so, they are recorded at 1599 ± 1, 1577, 1487, and 1442 cm^{-1} for the low W content samples, and at 1603, 1586, 1577, 1490, and 1444 cm^{-1} for samples WM24 and WMT24. These bands can be ascribed to modes 8a, 8b, 19a, and 19b of py coordinated to surface Lewis acid sites (Table 3). The spectra are rather similar to each other, whichever the support or the calcination temperature. As the W content is increased, the outgassing temperature required to remove the bands due to adsorbed py also increases, from 573 K for low W contents to 673 K for the high-loaded samples, indicating that the surface Lewis acid sites become stronger as the W content increases. The splitting of the band due to mode 8a, in some cases, samples WM24 and WMT24 (recorded at 1603 and 1586 cm^{-1}) indicates the presence of two types of surface Lewis sites. The band at 1586 cm^{-1} is usually ascribed to the adsorption of pyridine on weaker surface Lewis acid sites, as the bands shift toward higher wavenumbers as the strength of the surface site where the py molecules become bonded

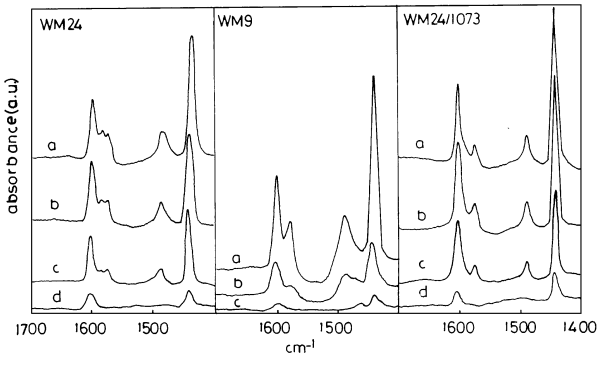

FIG. 12. FT-IR spectra recorded after adsorption of pyridine at room temperature on samples WM9, WM24, and WM24/1073, and outgassed at (a) room temperature, (b) 373 K, (c) 473 K, and (d) 573 K.

TABLE 3

Position (cm^{-1}) and Ascription of the FT-IR Absorption Bands Recorded after Adsorption of Pyridine on the Samples Studied

Sample	8a	8b	19a	19b
WM5	1598	1576	1487	1443
WM9	1599	1576	1487	1442
WM18	1599	1576	1487	1442
WM24	1603	1577	1490	1444
	1586			
WMT24	1603	1577	1490	1444
	1586			
WM24/1073	1603	1577	1490	1444
WM24/1273	1604	1577	1490	1444
	1586			

increases. Although this band could be also ascribed to physisorbed py, this ascription should be ruled out, as it is recorded (as a shoulder) even after outgassing the sample at 473 K; so, the band could be related to adsorption on coordinatively unsaturated Mg(II) cations existing in tungstates.

The spectra recorded for high-temperature calcined samples (WM24/1073 and WMT/1073) (Fig. 12) are also similar to those previously described for the lower W content samples calcined at 723 K (i.e., sample WM9). Bands due to coordinated py are recorded at 1603, 1577, 1490, and 1444 cm^{-1}. The bands are recorded even after outgassing the samples at 673 K, indicating that the adsorption sites are rather strong surface Lewis acid sites. The spectra for the samples calcined at the highest temperature (WM24/1273 and WMT24/1273) are similar to that for sample WM24, the band due to mode 8a (Table 3) being splitted into two maxima at 1604 and 1586 cm^{-1}.

It should be noted that no band due to formation of pyridinium species was detected in any case, indicating the absence of surface Brønsted acid sites.

3.7. Scanning Electron Microscopy

Parent MgO is formed by irregular particles (Fig. 13a). Incorporation of tungsten and calcination at 723 K leads to a change in the morphology of the particles, now showing a layered structure, typical of brucite, although X-ray diffraction data have shown that the sample contains periclase, and not brucite. This apparent disagreement can be overcome taking into account that the periclase–brucite phase change is pseudomorphic, and so the external shape of the particles is retained even after the transformation to periclase (Fig. 13b). Only after calcination at 1273 K, sample WM24/1273 (Fig. 13c), stick-shaped or rounded particles are detected, corresponding to $MgWO_4$(II) wolframite. These results further confirm the extreme dispersion degree or amorphous nature of the tungsten-containing phases of the samples, even with rather high tungsten loadings.

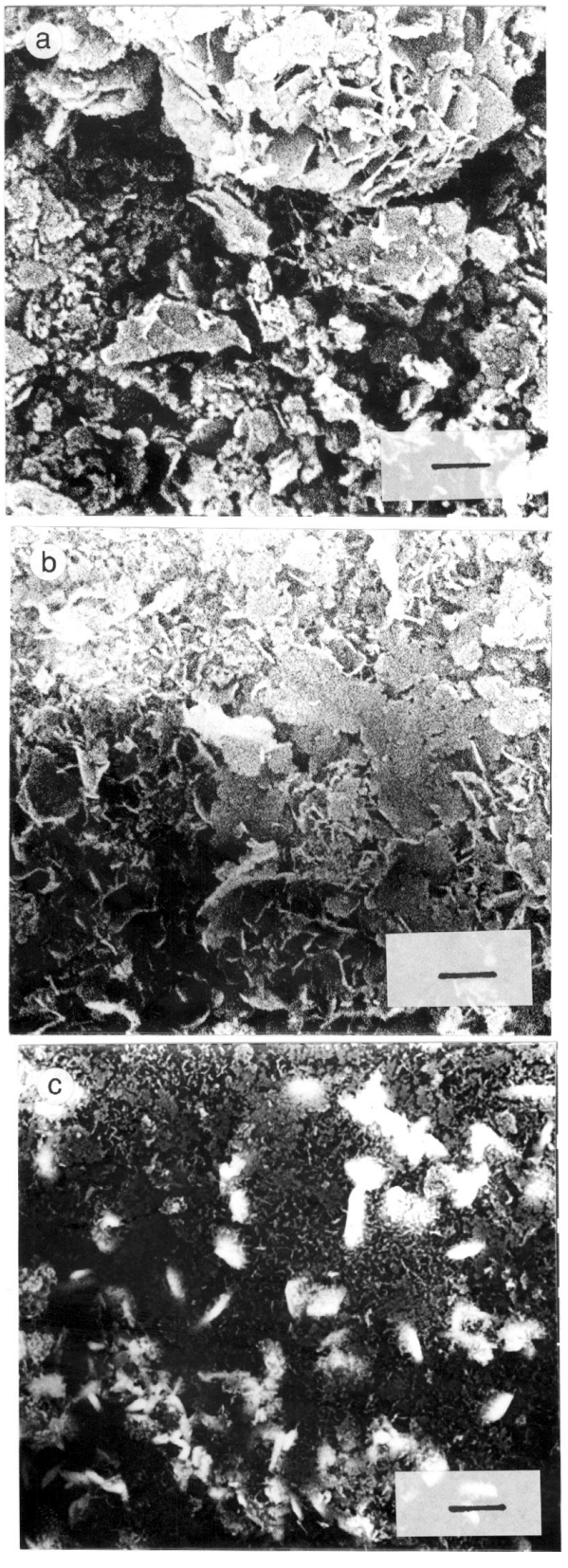

FIG. 13. Scanning electron micrographs for (a) MgO; (b) WM24/1073; (c) WM24/1273 (bar length, 1 μm).

4. CONCLUSIONS

The results obtained indicate that both the W content and the calcination temperature modify the nature and physicochemical properties of the phases formed on supporting tungsta on magnesia. The presence of water during preparation of the samples gives rise to high specific surface area solids, due to the reversible MgO (periclase) $\rightarrow$ $Mg(OH)_2$ (brucite) phase transformation. The use of one or another support does not modify the nature of the W-containing phases formed nor their reducibility or surface acid properties; the only change observed corresponds to the specific surface area, larger when starting from the brucite support.

X-ray diffraction, W L_3 EXAFS, and Raman spectroscopy results provide information about the nature and properties of the W-containing species formed. Crystalline tungstates exist in samples calcined at very high temperature. The major phase in sample WM24/1073 is $MgWO_4$(I), a magnesium tungstate where W is tetrahedrally coordinated. As the calcination temperature is increased, a different phase, $MgWO_4$(II), is formed, with the wolframite structure and octahedral [WO_6] species. For samples calcined at low temperature (723 K), amorphous magnesium tungstates are detected, for which the local environment of W cations coincides with that existing in $MgWO_4$(I) for low W content, but with that of wolframite, $MgWO_4$(II), for high loadings (24%). Such a change in the coordination of W species from [WO_4] to [WO_6] has been already reported for other systems (24). Formation of tungstates in all samples studied, even for those containing low W loadings and calcined at low temperature, should be due to the strong acid/base interaction between WO_4^{2-} and $Mg(OH)_2$.

Reducibility of W^{6+} cations is strongly inhibited by the formation of magnesium tungstates, being much lower than that observed either for bulk WO_3 or for tungsta supported on other metal oxides (silica, alumina, titania).

Incorporation of tungsten onto MgO increases surface acidity and develops surface Lewis acid sites (W^{6+}_{cus}), which strength increases as the W content increases. Two types of surface Lewis acid sites exist for W-rich samples calcined below 1073 K; the stronger one corresponding to W^{6+} cations, and the weaker one corresponds to Mg^{2+}.

ACKNOWLEDGMENTS

The authors thank DGICYT for financial support (Grant PB93-0633). G.S. acknowledges a sabbatical leave from Universidad de Guanajuato (México). Thanks are given to Daresbury Laboratory for allocating beam time for XAS measurements (Grant 25/359).

REFERENCES

1. Salvatory, L., Makousky, L. E., Stenciel, J. M., Brown, F. R., and Hercules, D. M., *J. Phys. Chem.* **85**, 3700 (1981).
2. Ahmed, A., *Bull. Soc. Chim. Fr.* **127**, 179 (1990).
3. Moffat, A. J., Clark, A., and Johnson, M. M., *J. Catal.* **22**, 379 (1971).
4. Ai, M., *J. Catal.* **49**, 305 (1977).

5. Yamaguchi, T., Tanaka, Y., and Tanabe, K., *J. Catal.* **65**, 442 (1980).
6. Hattori, H., Asada, N., and Tanabe, K., *Bull. Chem. Soc. Jpn.* **51**, 1704 (1978).
7. Thomas, R., van Oers, E. M., de Beer, V. H. J., Medema, J., and Moulijn, J. A., *J. Catal.* **76**, 241 (1982).
8. Cortés, A., and Seoane, J. L., *J. Catal.* **34**, 7 (1974).
9. Hanuza, J., Jezowska-Trzebiatowska, B., and Oganowski, W., *J. Mol. Catal.* **29**, 109 (1985).
10. van Roosmalen, A. J., Koster, D., and Mol, J. C., *J. Phys. Chem.* **84**, 1075 (1980).
11. Chan, S. S., Wachs, I. E., Murrell, L. L., and Dispenziere, N. C., Jr., *J. Catal.* **92**, 1 (1985).
12. Thomas, R., Kerkhof, F. P. J. M., Moulijn, J. A., Medema, J., and de Beer, V. H. J., *J. Catal.* **61**, 559 (1980).
13. Tinttarelli, P., Iannibello, A., and Villa, P. L., *J. Solid State Chem.* **37**, 95 (1981).
14. Uurman, M. A., and Wachs, I. E., *J. Phys. Chem.* **96**, 5008 (1992).
15. Sayers, D. E., and Bunker, B. A., *in* "X-Ray Absorption: Principles and Aplications of EXAFS, SEXAFS and XANES" (D. C. Koningsberger and R. Prins, Eds.). Wiley, New York, 1988.
16. Mustre de León, J., Rehr, J. J., Zabinsky, S. I., and Albers, R. C., *Phys. Rev. B* **44**, 4146 (1991).
17. de Boer, J. J., *Acta Crystallogr. B* **30**, 1878 (1974).
18. Malet, P., and Caballero, A., *J. Chem. Soc., Faraday Trans.* **84**, 2369 (1988).
19. Sing, K. S. W., Everett, D. H., Haul, R. A. W., Moscou, L., Pierotti, R. A., Rouquerol, J., and Sieminiewska, T., *Pure Appl. Chem.* **57**, 603 (1985).
20. Volpe, L., and Boudart, M., *Catal. Rev.-Sci. Eng.* **27**, 514 (1985).
21. Llorente, J. M. M., and Rives, V., *Solid State Ionics* **50**, 59 (1992).
22. Chang, L. L. Y., Scroger, M. G., and Phillips, B., *J. Am. Ceram. Soc.* **49**, 385 (1966).
23. Gunter, J. R., and Dubler, E., *J. Solid State Chem.* **65**, 118 (1986).
24. Horsley, J. A., Wachs, I. E., Brown, J. M., Via, G. H., and Hardcastle, F. D., *J. Phys. Chem.* **91**, 1014 (1987).
25. Thomas, R., Mittelmeijer-Hazeleger, M. C., Kerkhof, F. P. J. M., Moulijn, J. A., Medema, J., and de Beer, V. H. J., *in* "Proceeding Climax Third International Conference on the Chemistry and Uses of Molybdenum" (H. F. Barry and P. C. H. Mitchell, Eds.), p. 85. Climax Molybdenum Co., Ann Arbor, MI, 1979.
26. Filipenko, O. S., Pobendiskoya, E. A., Ponomareva, V. I., and Bolov, N. V., *Krystallogr.* **13**, 1073 (1968).
27. Ogata, E., Kamiya, Y., and Ohta, N., *J. Catal.* **29**, 296 (1973).
28. Thomas, R., van Oers, E. M., de Beer, V. H. J., and Moulijn, J. A., *J. Catal.* **84**, 275 (1983).
29. Martín, C., Martín, I., and Rives, V., *J. Mol. Catal.* **73**, 51 (1992).